Soft Matter

PAPER

Check for updates

High-throughput microscopy to determine morphology, microrheology, and phase boundaries applied to phase separating coacervates†

Yimin Luo, [ab] Mengyang Gu, [c] Chelsea E. R. Edwards, [a] Megan T. Valentine [*b] and Matthew E. Helgeson [*a]

Evolution of composition, rheology, and morphology during phase separation in complex fluids is highly coupled to rheological and mass transport processes within the emerging phases, and understanding this coupling is critical for materials design of multiphase complex fluids. Characterizing these dependencies typically requires careful measurement of a large number of equilibrium and transport properties that are difficult to measure *in situ* as phase separation proceeds. Here, we propose and demonstrate a high-throughput microscopy platform to achieve simultaneous, *in situ* mapping of time-evolving morphology and microrheology in phase separating complex fluids over a large compositional space. The method was applied to a canonical example of polyelectrolyte complex coacervation, whereby mixing of oppositely charged species leads to liquid–liquid phase separation into distinct solute-dense and dilute phases. Morphology and rheology were measured simultaneously and kinetically after mixing to track the progression of phase separation. Once equilibrated, the dense phase viscosity was determined to high compositional accuracy using passive probe microrheology, and the results were used to derive empirical relationships between the composition and viscosity. These relationships were inverted to reconstruct the dense phase boundary itself, and further extended to other mixture compositions. The resulting predictions were validated by independent equilibrium compositional measurements. This platform paves the way for rapid screening and formulation of complex fluids and (bio)macromolecular materials, and serves as a critical link between formulation and rheology for multi-phase material discovery.

a Department of Chemical Engineering, University of California, Santa Barbara 93106, USA. E-mail: helgeson@ucsb.edu

b Department of Mechanical Engineering, University of California, Santa Barbara, USA. E-mail: valentine@engineering.ucsb.edu

c Department of Statistics and Applied Probability, University of California, Santa Barbara, USA

† Electronic supplementary information (ESI) available: Tables S1–S2; Fig. S1–S8. See DOI: 10.1039/d1sm01763b

1 Introduction

Phase separating complex fluids including polymer solutions and blends,[1] colloidal dispersions and gels[2,3] are important for the processing of many soft materials. Technologically-relevant examples include biophotonic nanostructures[4] and polymer membranes.[5] Key to these processes is the complex interplay between the evolving composition of the emerging phases and their rheology,[6,7] which sets the balance between the advection of phase separation and its resistance by viscous dissipation or elasticity, and determines the kinetics by which multi-phase morphologies emerge and coarsen over time.

Often, the characterization of such kinetically-evolving, multi-phase materials is hampered by the difficulty in sampling the compositions and properties of the emergent phases and structures as they evolve in real time. A common approach is to separate the phases using external forcing (*e.g.*, sedimentation) in order to measure their composition, structure and rheology. However, this *ex situ* approach is invasive, as it necessarily interrupts the phase separation process. Moreover, this approach can require large material volumes, and is sacrificial as the material is often destroyed during the measurement.[8] These challenges have limited experimental investigations and hampered our understanding of the relationships between composition and rheology for a wide range of phase separating materials.

An industrially-relevant,[9,10] contemporary example is the complex coacervation of polyelectrolyte solutions, in which oppositely charged macroions form polyelectrolyte complexes (PECs)

that can undergo charge condensation-driven liquid–liquid phase separation (LLPS) into a PEC-rich dense coacervate phase and a PEC-lean dilute solution.[11,12] As studies of the dense phase properties usually involve phase separation from a relatively dilute solution,[13,14] a small perturbation in the initial composition often translates to dramatically different dense phase composition. As a result, the connection between dense phase rheology and phase separation remains incompletely understood. This challenge is compounded by the difficulty in characterizing coacervates with conventional methods. Specifically, isolating and analyzing the small volume of dense phase is typically time consuming. Further, recent work shows that the presence of arrested states and time to equilibration is strongly controlled by both the order of polyelectrolyte addition[15] and the mixing mechanics.[16] Meanwhile, although it is common to assume that neither the processing[16] nor the subsequent isolation[17] affect the composition of the dense phase, which is assumed to be located on the equilibrium phase boundary, this assumption has rarely been validated with independent measurements.

Recent work on coacervates has examined connections between viscoelasticity and salt concentration,[18] pH,[19] mixing stoichiometry[20] and chain length[21] of phase separated coacervates through time-composition superposition.[22,23] These experiments are painstaking, as they involve separation of the dense and dilute phases at sufficient volume for conventional rheological measurements.[17,24] As a result, the question of how rheology evolves with the ongoing phase separation remains unclear.[16] These previous studies were also largely limited to the region of

the phase diagram where the viscosity was sufficiently high so that the rheology can be resolved by conventional bulk rheometry.[17,18,24,25] By contrast, bulk rheometry is inaccessible to low viscosity systems and in cases where materials are scarce, such as peptides[26,27] and proteins,[28] which are often used to study the charge-sequence dependence of polyelectrolyte coacervation.[29,30] There is therefore a considerable need for *in situ*, high-throughput characterization tools to simultaneously resolve the morphological, rheological and phase boundary information on coacervates and other phase separating complex fluids over wide range of phase diagram parameters and in time, thereby circumventing the need for the types of time-consuming experiments conventionally associated with such systems.

In this work, we develop a method for *in situ* observation of evolving morphology, composition and rheology of phase separating complex fluids based on high-throughput optical microscopy and passive probe microrheology measurements,[31,32] and use it to quantify phase separation in polyelectrolyte mixtures during complex coacervation. Our workflow (Fig. 1) is composed of a high throughput data acquisition block that is material-agnostic (left) and an analysis block that is material-specific (right). The data acquisition block couples a motorized stage with automated image acquisition routines that are adapted for conventional well plates. This platform allows systematic acquisition of image and dynamic video datasets for determination of phase morphology and rheology for a wide range of compositional formulations using minimal sample volumes, without the need
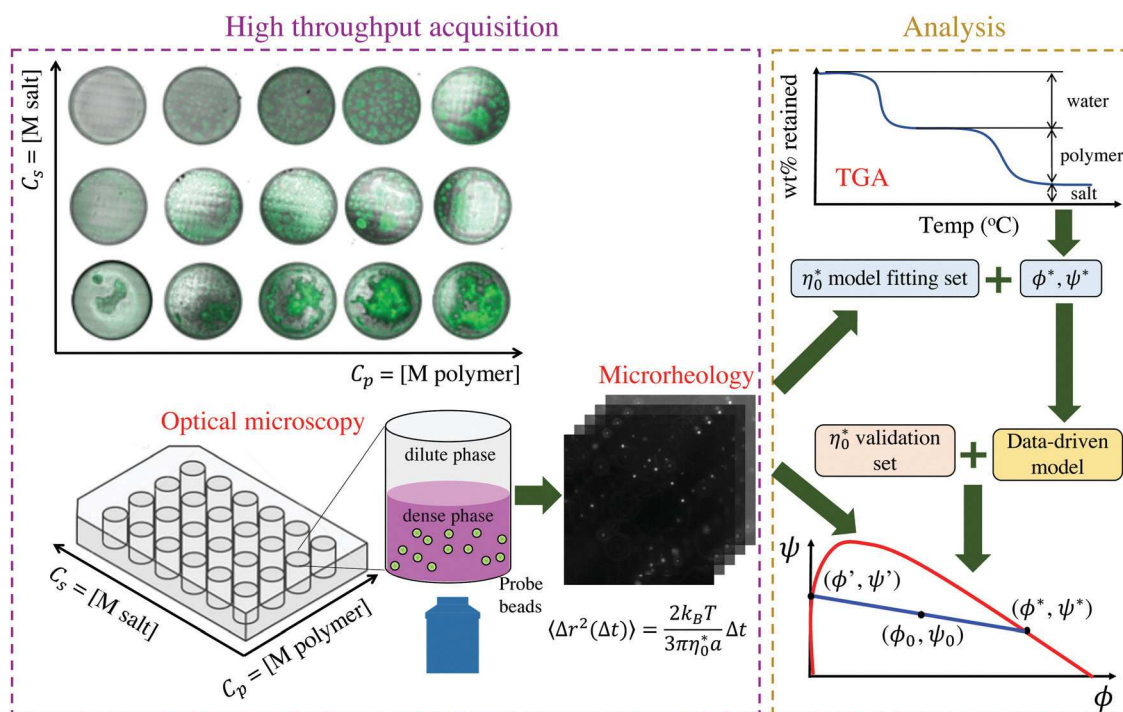

Fig. 1 A sketch of the process flow diagram of our data-driven approach. High-throughput microrheology is used to obtain the morphology and viscosity η_0^* of the PEC-rich phase from an initial composition (C_p, C_s). The viscosity data are then split into model fitting and validation sets. The data in the model fitting set, in combination with TGA measurements, are used to determine the relationship between the composition and the viscosity of the PEC-dense phase. This relationship is then used to reconstruct the phase boundary and the tie line using the viscosity from the validation set.

for individually mounting or manually scanning samples. As such, this approach can be used to non-invasively monitor materials *in situ* as phase separation progresses.[33–35] Microrheology is particularly suited to characterizing systems with low viscosity, such as those obtained from initially dilute mixtures.[36] We chose to apply our analysis to map the equilibrium phase boundary, which is predicated on equilibrium being established. Compositions were determined by a secondary method to validate the data.

The manuscript is organized as follows: we first report the selection and development of a model test system involving coacervating polyelectrolyte mixtures. We then demonstrate the ability of the method to resolve morphology and microrheology information to high precision in regions of low viscosity and over long periods of time that were inaccessible to previous methods. In particular, this approach allows us to probe evolving viscosity of the dense phase during phase separation in a noninvasive manner. Finally, we show that the large datasets provided by the high throughput method enable a new avenue for data-driven analysis, in which the mapping of viscosity to fluid composition can be used to estimate key features of the equilibrium phase diagram of the phase separating systems without the need for independent composition measurements.

2 Material and methods

2.1 Preparation of polyelectrolyte complexes for wellplate scanning

Poly(acrylic acid, sodium salt) solution (PAA, degree of polymerization N = 160, molecular weight = 15 kg mol^{-1}) and poly(allylamine hydrochloride) powder (PAH, degree of polymerization N = 187, molecular weight = 17.5 k g mol^{-1}) were purchased from Sigma Aldrich, and used without further purification. 2 M (in base pairs) stock solutions of charged macromolecules and their associated counter-ions were prepared. A stock solution of PAH was prepared by weighing out powder, adding deionized water (Milli-Q, 18.3 MΩ) at the desired volume, and stirring with a magnetic stir bar to obtain a clear solution. A PAA stock solution was diluted from a 35 wt% solution, as supplied by the manufacturer.

Mixing of the polyelectrolytes was carried out inside 96-Well Krystal Glass Bottom Imaging Plates (Thomas Scientific, Swedesboro, NJ), where each well can hold a maximum of 360 μL. Each sample had a total volume of 300 μL, and the compositions were formulated by molar concentration, C_p and C_s of polymer and salt, respectively. The added polymer C_p includes charged macromolecules and their associated counter-ions. Polyelectrolyte complexes were prepared at a 1:1 stoichiometric charge ratio of polycations and polyanions, by assuming complete dissociation of charged monomers and mixing equal volume of equimolar polyelectrolyte stock solutions (=2 M). For instance, a sample formulated with an added polymer concentration of C_p = 100 mM contains not only 50 mM of poly(acrylic acid) and poly(allylamine), but also 50 mM of Na and HCl counter-ions, in addition to added salt C_s.

The mixing order proceeded as follows: a NaCl stock solution (5 M) was first diluted with deionized water and a suspension of 0.01 vol% pre-washed, yellow-green fluorescent carboxylated particles (2a = 1 μm Polysciences, Warrington, PA) in Milli-Q water, and triturated by pipette three times to fully mix the solution. The volume of particles added is proportional to the polyelectrolyte stock solution. This way, the particle volume fraction in the dense phase Φ_p is similar the dense phase in each sample ($\Phi_p \approx 1 \times 10^{-4}$). Required amounts of PAA stock solutions were then added to solutions containing the desired amount of deionized water, NaCl stock solution and particles, and triturated by pipette twice to fully mix the solution. Finally, the required amounts of PAH stock solutions were added. After mixing all desired components, the entire well plate was sealed with parafilm (Bemis Company, Neenah, WI), secured with tape, and capped with a lid to minimize evaporation. The well plate was wrapped in aluminum foil and left to equilibrate prior to imaging. Although phase separation can be accelerated by centrifuging,[14] we found that it can sometimes lead to sedimentation and aggregation of probes in lower viscosity samples, and thus we instead chose to let the dense phase to settle to the bottom into one continuous phase by gravity.

2.2 Thermogravimetric analysis

Dilute and dense phase compositions were determined by a thermogravimetric furnace method following previously published protocols[13,14] using a Ney Vulcan 3-1750 Box Furnace. Briefly, 2.5–10 mL of polyelectrolyte solution, at 3 polymer concentrations (C_p = 100, 600 and 1000 mM) and 4 salt concentrations (C_s = 3–4.5 M at 0.5 M increments), were mixed without adding any fluorescent particles. The two phases were recovered by centrifuging (2000 rpm, 30 min) and decanting the dilute supernatant to separate the phases. Three replicate samples of each phase, each with a volume of roughly 50 μL, were prepared for each formulation, and loaded into aluminum pans. Each pan was weighed before and after loading to determine the initial solution mass. A timed sequence of temperature steps was used to selectively eliminate various components. In the first step, the samples were heated to 110 °C and held for 2.5 hours to evaporate water. In the second step, the samples were heated to 600 °C and held for 12 hours to pyrolyze and evaporate the polymers, leaving only salt. After each step, the weight of the pan was recorded for every sample. The volume fraction of polymer, salt and water were calculated using the following density values, as in:[14] ρ_w = 1 g mL^{-1}, ρ_{polymer} = 1.3308 g mL^{-1}, and ρ_{NaCl} = 2.16 g mL^{-1}. Three replicates were made for both the dilute and dense phase of each initial composition.

Throughout the text, for coacervation in the salt-polymer phase diagram, we use superscripts "*" and "′" to denote material properties and compositions for the PEC-dense and PEC-dilute branches of the phase boundary, respectively, and subscript "0" for those related to the initial mixture in the two-phase region. C_p and C_s refer to the molar concentrations of polymer and salt, while ϕ and ψ refer to the volume fractions of same. All other units are explicitly stated.

2.3 Automated optical microscopy

Samples were imaged using a Zeiss Axio Observer 7 microscope outfitted with a computer-controlled motorized sample stage and motorized auto-focus objectives, and recorded with an Axiocam 702 monochromatic camera. The location of each well within the plate was first calibrated following standard procedures in the Zeiss ZEN software to record the position of the wells. Tiling of imaging regions within each well was performed using a $10\times$ objective (NA = 0.3, magnification = 590 nm per pixel). A tiled region was designated around each well, which consisted of 77 tiles with a 20% overlap between them. A sequence of scans was automatically carried out, and tiles were labeled by the well number. A single channel image of each well took roughly one minute to scan. Afterwards, the sequence of images was labeled by the well number. Finally, multiple fields of view were merged using the Processing Module in ZEN to render a stitched image of each well.

To acquire image stacks for microrheology, we used an oil-immersion, $63\times$ objective lens (NA = 1.4), which with the chosen camera resolution provides a magnification of 93 nm per pixel. The samples were imaged in fluorescence mode to maximize the signal-to-noise ratio, using a Colibri 7 light source and standard GFP filter set. A single field of view (960 pixels $\times$ 960 pixels) was designated in each well, and a time series was acquired, using a 5 ms exposure and a 10 Hz frame rate.

2.4 Microrheology procedures

2.4.1 Probe selection. Several particle surface chemistries were screened to determine their preferential partitioning into each phase. We found that polystyrene (PS) particles grafted with methoxy-terminated PEG (mPEG, 2 kg mol^{-1}) selectively partitioned to the dilute phase, those grafted with acrylate-terminated PEG (3.4k) partitioned to the fluid–fluid interface, and carboxylated PS particles partitioned to the dense phase. In the final case, the probes were estimated to contribute negligibly to the ionic strength of the system (Note 1.2, ESI†). The selection of probes that partition to the phase to be characterized by microrheology (in this case, the dense phase) ensures that the other phase(s) contributes little signal to the image stack used for microrheology analysis.

2.4.2 Multiple particle tracking (MPT). The particles were tracked using an open source tracking algorithm.[37,38] In brief, the algorithm finds the centroid position of each particle in each frame and then links these positions across frames to generate trajectories of individual particles as a function of time. In order to determine the localization noise floor (*i.e.*, the static error), which defines the minimum resolvable displacement, control experiments were first performed for particles immobilized in a stiff polyethylene glycol-based hydrogel (Fig. S2, ESI†) under the same sample geometry and imaging conditions, as previously described.[39] After obtaining all particle trajectories using MPT, the mean squared displacement (MSD) at each lag time, Δt, is computed as the mean of the squared, 2D displacement over all particles and over all starting times t: $\langle \Delta r(\Delta t) \rangle = \langle (x(t + \Delta t) - x(t))^2 + (y(t + \Delta t) - y(t))^2 \rangle$.

The variance is also computed as the standard deviation of these mean squared displacements. The static noise floor, an intrinsic error in determining a particles' position due to inherent noise in the measurements,[40] adds a small offset value to the measured particle dynamics, and thus causes an artificial plateau in $\langle \Delta r^2(\Delta t) \rangle$ at sufficiently small Δt.[41] In order to avoid this artifact, the static noise floor value, once determined by tracking immobilized particles, is subtracted from all $\langle \Delta r^2(\Delta t) \rangle$.[31,34,41] We find that the MSD increases linearly with lag time for the range of lag times probed (0.1–10 s), which correspond to the angular frequency range $\omega = 0.63$–6.3 rad s^{-1}. This indicates a predominantly viscous material response in this frequency range.

The smallest time and length scales accessible by this method are limited by microscope acquisition framerate and resolution limits. In general, using $2a = 1$ µm probe particles, the probed length scale ranges from 10 s of nm to 10 s of µm, and the timescale ranges from 0.01 to 10 s of seconds.[31] Stiff (>10 s of Pa) or very viscous materials (>10 s of Pa s) are difficult characterize by this method because of small probe displacements. For the analysis – which assumes that probes experience a locally homogeneous material – to be applicable, the length scale of non-homogeneous phases and concentration fluctuations must be significantly larger than the probes, which ranges from hundreds of nm to several µm. Since the MSD statistics are averaged over all particles and all frames, spanning 10 s of seconds, it is assumed that the system is ergodic: that the probes will sample all states uniformly and randomly, so the averaged viscosity derived from the ensemble of particles is the same as averaging individual trajectory over longer times. We typically observe about 30–40 particles in each frame. Thus, the microrheology properties obtained using 20% of Δt will be the result of averaging 20 000 particle-steps, sufficient for viscosity determination of a homogeneous sample. The process is also assumed to be stationary within the window of the measurement.

2.4.3 Fitting procedure to determine viscosity. To avoid the bias introduced at large Δt from limited statistics, only the first 20% of the Δt's are used in the fit to extract the viscosity across all samples (interested readers are referred to Note 2.5 in ESI† for a sensitivity analysis for the effect of different truncations). Each MSD is weighted by the inverse of the variance in fitting the linear model with 0 intercept to obtain the slope, which in two dimensions is equal to $4D$, where D is the diffusion coefficient. The viscosity η is found by the Stokes–Einstein relation

$$\eta = \frac{k_B T}{6\pi a D}$$

where k_B is the Boltzmann constant, T is the absolute temperature, and a is the particle radius.

3 Results and discussion

3.1 Selection & parametrization of the model coacervating system

To demonstrate our ability to acquire *in situ* morphological and rheological information simultaneously during phase separation,

we select a well-characterized PEC-forming polyelectrolyte pair: poly(acrylic acid, sodium salt)(PAA)–poly(allylamine hydrochloride) (PAH). This polymer pair was chosen because of its large two-phase coacervate region, and the wealth of literature on its macroscopic equilibrium phase behavior, structure, and viscoelastic properties.[14,17,36,42]

We first quantify the phase behavior in the composition range spanning the region of coacervation by acquiring data at previously unreported elevated added salt concentrations (≥ 3 M), as shown in Fig. 2, following published protocols.[14] We also perform an important set of validative experiments that has not previously been reported, by performing the TGA on the separate stock polyelectrolyte solutions individually (ESI†) and verifying that the analysis reproduces the known polymer concentration in the stock solution. We find that, in the case of PAH, the wt% of polymer is consistent with the weight change in the pyrolyzing step; in the case of PAA, the formation of Na_2CO_3 causes an apparent increase in remaining wt% after the pyrolyzing step; once we account for the additional wt% from the $-CO_3$ moeity, the wt% is consistent with the known concentration in the stock solution, thus providing confidence in the concentrations we report.

The resulting phase diagram is first presented in wt% of the components (Fig. 2b), obtained by weighing the sample directly. The system exhibits negatively sloped tie lines, *i.e.*, the small counter-ions of the polyelectrolytes preferentially concentrate in the polymer-depleted dilute phase. Voorn–Overbeek theory,[43] which takes into account both the entropy of mixing and simple Debye–Hückel type screened electrostatic interactions, predicts positively sloped tie lines, whereas later work found that the excluded volume of small ions must be added to account for the negatively sloped tie lines often observed in experiments.[13,14] More recently, it has been shown[44] that the direction of salt partitioning is not universal, but rather depends both on the polyelectrolyte sequence chemistry and charge density.[44]

Since the added polymer concentration C_p is inclusive of the polyelectrolytes and their counter-ions, the latter also contributes extra ions to the system. During PEC formation, the fraction of counter-ions released by the polyelectrolyte-salt complexes is termed the degree of ionization, α,[17,36] which depends not only on the dissociating strength of the polyelectrolytes but also the charge environment, and influences the tie line connecting compositions of the dense phase $\left(C_p^*, C_s^*\right)$ and dilute phase $\left(C_p', C_s'\right)$ on the phase diagram. α therefore relates the formulation composition (C_p, C_s) to the initial concentration $(C_{p,0}, C_{s,0}) = (C_p, C_s + \alpha C_p)$. We note that incomplete ionization contains contributions from both counter-ion binding and pH-dependent protonation. Consequently, an accurate value of α is crucial to obtaining the correct dense and dilute phase compositions using TGA.

For strong polyelectrolytes such as the ones used in this study, it is generally assumed that the degree of ionization $\alpha = 1$; however, as shown in Fig. 2c, we find that this is not the case for the region of the phase diagram explored here. The exact value of α is less important for regions of lower salt concentration where the salt concentration of the dense phase is insensitive to the total polymer concentration (*i.e.*, the region with $\psi < 0.05$ where the dense phase boundary is approximately vertical), but plays an important role in the region closer to the critical point where the location of the phase boundary is sensitive to salt concentration. The specific value of α and its influence on apparent phase behavior has not been carefully explored in earlier works; here, we present a systematic analysis by which it can be estimated from TGA measurements across a wide composition range (Note 6.1, ESI†).

We note that while $\alpha = 1$ sufficiently describes the data at low salt concentrations (1–2 M, dark green state points and tie lines in Fig. 2c, where "x" is computed by $\alpha = 1$), we find that a smaller α better describes the region with higher added salt (≥ 3 M, black state points). In principle, plotting the initial mixture compositions prior to phase separation in this representation should produce state points that lie along the common tie line. However, this will only be the case for the correct value of α; an incorrect value of α will produce deviations
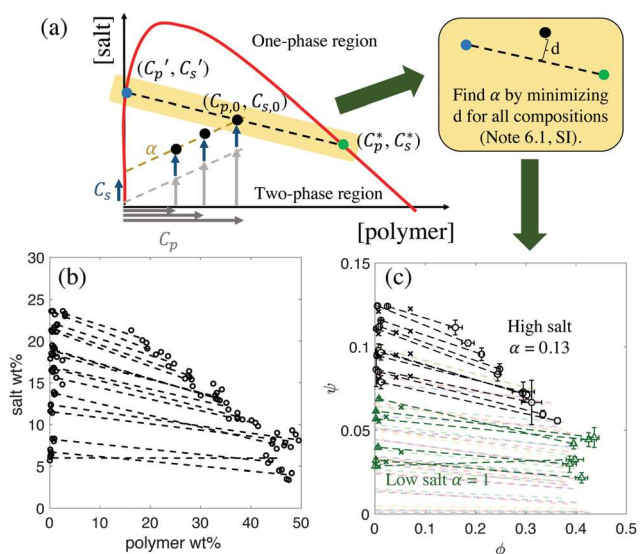

Fig. 2 Determination of equilibrium phase diagram obtained from TGA. (a) Sketch of the phase diagram and how it is populated based on initial compositions $(C_{p,0}, C_{s,0})$ and the equilibrium PEC-dilute $\left(C_p', C_s'\right)$ and PEC-dense $\left(C_p^*, C_s^*\right)$ phase compositions they produce within the two-phase region for a given extent of ionization, α. The yellow shaded box highlights a single tie line which is transformed for the optimization. (b) Measured phase diagram where all experimental measurements are represented in wt%. The tie lines, denoted by the dashed lines, are constructed by connecting the average of the replicate measurements for the dense and dilute phase. (c) The data in (b) are converted to volume fraction using densities. An optimization procedure to minimize the distance d from the initial composition to the tie line was used to determine the optimal value of $\alpha = 0.13$ (black data). The dark green data were performed at lower added salt (1–2 M) for overlapping measurements but were not used for fitting, where $\alpha = 1$. Error bars represent standard deviations of replicate measurements. The data are superimposed on the tie lines obtained from previously reported TGA measurements of the same system (compositions not shown) in semi-transparent dashed lines, reproduced from ref. 14.

between the collection of initial state points and the tie line. An apparent value of $\alpha = 0.13$ can therefore be obtained by minimizing the aggregate error between the distribution of initial compositions and the normalized tie line (for detailed calculation procedures, see Note 6 and Fig. S9 in ESI†). We hypothesize that such a low apparent fractional charge of the polyelectrolytes, which we recall includes both counter-ion binding and protonation of acidic charge groups, is due to the high ionic strength environment of the dense phase, differences in the pH between the initial solution and the separated phases, or both.

Finally, we compare the phase diagram in volume fraction (Fig. 2c) determined from the present experiments to previously published data,[14] including the tie lines obtained by TGA measurements of the same system. We find excellent quantitative agreement in regions of comparable salt concentration. This validates the scheme for selecting α, and allows the present data to extend the determination of the phase boundary for coacervation to higher salt concentrations toward the critical point. We note that extrapolation of the phase boundary to the critical point produces a critical salt concentration above the saturation concentration for NaCl, consistent with our experimental observations (not shown) that coacervate droplets are visible in optical microscopy at saturated NaCl below 10 μM polyelectrolyte.

3.2 Tracking time evolution of phase separation by *in situ* microscopy

To demonstrate the capabilities of the high-throughput automated microscopy system described previously, we perform experiments to track the progression of phase separation upon mixing into the two-phase region determined in Fig. 2. The combination of spatially mapped imaging and passive probe microrheology enables these experiments to track changes in morphology during kinetic evolution of phase separation by coacervation, while simultaneously measuring spatially-addressed microrheology to characterize the transient material properties that develop during the process *in situ*. Compositions from the two-phase region are initially mixed on a 96-well plate, and each well is imaged in its entirety over time by stitching together tens of fields of view using automated scanning. This approach avoids the selection bias that can arise when different isolated locations are imaged within each well. Moreover, the approach differs from previous studies that track the progression of coacervation *via* measurement of turbidity,[15,36,45,46] which we find is an imprecise measure of scattering from coarsening coacervate droplets whose interpretation suffers both from resolution limitations as well as a signal that is sensitive to a convolution of droplet size distribution, internal composition and volume fraction. By contrast, our approach offers direct visualization of microscopic structural rearrangements, even long after macroscopic separation has occurred. Here, we show that high-throughput automated microscopy enables unique insight into how coacervate aging depends on its composition, and how microrheology can be used to sensitively assess whether phase separation is ongoing,

even when coarsening is undetectable from visual inspection of a time series of images.

Experimentally, we find that phase separation occurs in roughly four stages after the polyelectrolyte solutions are mixed (Fig. S8, ESI†): (I) the initial phase instability forms dispersed coacervate droplets; (II) the droplets sediment towards the bottom of the well plate under gravity; (III) the droplets coalesce to form larger droplets and eventually a continuous dense phase; and (IV) any dilute phase droplets trapped inside the continuous dense phase during coalescence continue to coarsen *via* coalescence. We find that stages I–III occur rapidly over the course of seconds to minutes, while Stage IV tends to proceed slowly over days to weeks, depending on the coacervate composition. As expected for phase separation with rheological asymmetry between the emerging phases,[47] the morphological and kinetic features of this phase separation are intricately coupled to viscoelastic properties of the dense phase. Thus, we next seek to explore effects of varying the amount of added salt on the evolving morphology, since the coacervate dense phase viscosity thins with increasing salt concentration.[17,18,25]

The rate of phase separation is highly coupled to the viscosity of the dense phase; the higher the viscosity, the more slowly phase separation occurs. We find that samples with higher added salt (Fig. 3a–d) have lower viscosities, consistent with prior reports.[17,18,25] In those cases, the phase separation occurs within minutes, after which the overall morphology remains unaltered for weeks (Fig. 3b). By contrast, samples with low added salt (Fig. 3e–h) can take several weeks or more to completely phase separate under gravitational sedimentation. Fig. 3f–h illustrates this slow evolution of phase separation over the course of three weeks. Micrographs recorded at the same time for two samples at high and low added salt indicate the difference in microscopic morphologies (Fig. 3a and e), which echos the trend in the measured phase boundary (Fig. 2), where samples with lower added salt concentration tend to contain higher concentration of polymer in the dense phase; these samples tend toward slower coarsening kinetics and more irregular interfaces indicative of slowly relaxing rheological response.

Although the sample morphology appears to quickly equilibrate for higher added salt concentrations, the PEC-dense phase still exhibits internal relaxation up to several days after mixing. This is evident in subtle trends in the observed microrheology, and is illustrated in Fig. 3c and d by measuring the mean-squared displacement (MSD) of probes localized to the dense phase within the same sample at various aging times ranging from 1–3 days after mixing, respectively. Specifically, at earlier aging times ($t = 22$ and 36 h), a subtle but clear transition is evident from diffusive scaling of the MSD ($\langle \Delta r^2(\Delta t) \rangle \sim \Delta t^1$) at short lag times to convective scaling ($\langle \Delta r^2(\Delta t) \rangle \sim \Delta t^2$) at long lag times (Fig. 3c). While such weak convection could potentially be due to thermal drift of the imaging system over time, the convective feature in the MSD disappears after sufficiently long aging times (Fig. 3d), ruling out this possibility. Therefore, we conclude that the observed long-time convective scaling of the MSD is due to the ongoing coarsening processes of Stages III and IV described previously. The processes of coalescence in
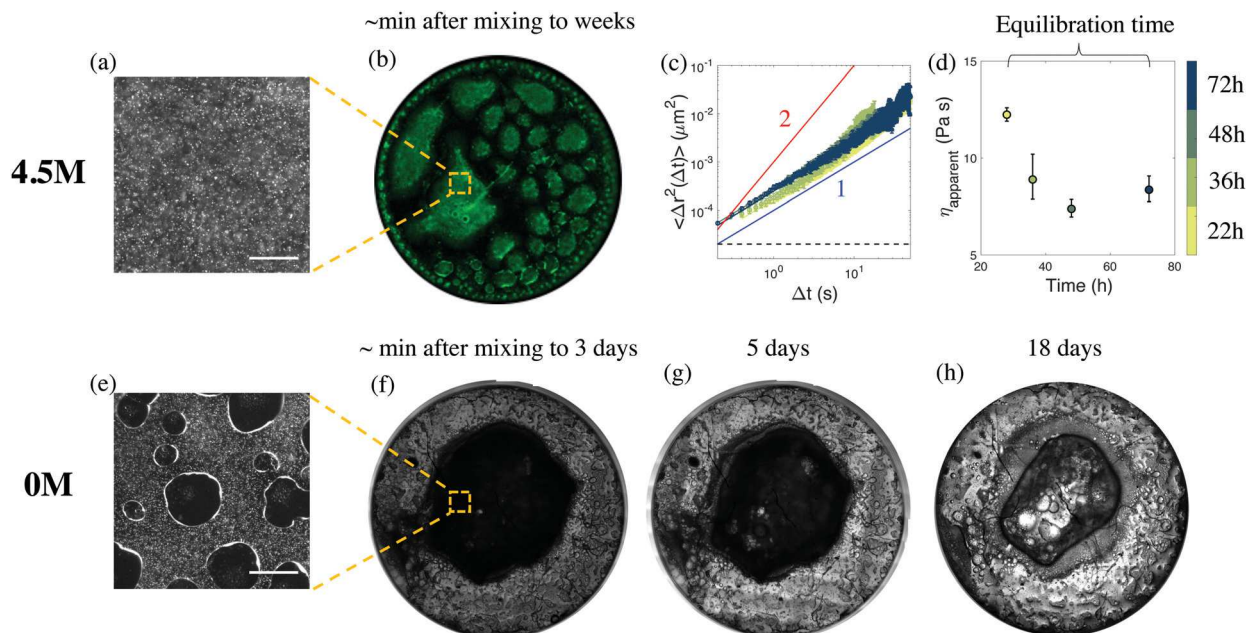
Fig. 3 Time evolution of the PEC morphology. Samples were prepared from an initial composition C_p = 100 mM total repeat units and C_s = 4.5 M added salt in (a–d) and C_p = 0 M added salt in (e–h). (a and e) Show fluorescence micrographs, where the signal comes from fluorescent particles in the PEC-dense phase. The scale bars are 100 μm. (b and f–h) Show images of the an entire well of radius = 7 mm, obtained by fusing 77 tiles collected using a 10× objective and a motorized stage. (c and d) Show MSDs and apparent viscosity acquired at different time points after mixing. The earlier MSDs in (c) show transient behavior that appears to approach a log slope of 2 at larger Δt, consistent with convective motion at long times. (f–h) Show Stage IV coarsening over long periods of time for a sample prepared with no added salt.

these stages cause interfacially-driven flows that propagate into the bulk dense phase, therefore contributing the observed convection to the probe motion. We note that the small magnitude of the convective velocity, which is barely discernible above the diffusive motion in some cases, would not be evident from tracing the trajectories of individual probe particles. Upon fitting a two-parameter diffusive convective model to the MSD: $\langle \Delta r^2(\Delta t) \rangle = (\bar{v} \, \Delta t)^2 + 4D\Delta t$, where $\bar{v}$ denotes the average convective velocity, we extract an apparent age-dependent viscosity during phase coarsening (Fig. 3d). We find that the apparent viscosity decreases with increasing aging time as coarsening proceeds. We note that measurements at different heights within the PEC-dense phase exhibit indistinguishable MSDs (ESI,† Note 2.4), suggesting that this variation is not due to concentration heterogeneities within the dense phase, but could instead be due to other rheological aging processes. A detailed study of how local concentration fluctuations give rise to evolving rheological behavior is beyond the scope of this work. Nevertheless, the present measurements demonstrate that the statistical information provided by microrheology analysis can serve as a highly sensitive probe of the kinetics of ongoing phase separation compared to other measures, including turbidity,[15] light scattering and even the analysis of structure within the microscopy images themselves. The convection observed at large lag times Δt as the phases undergo restructuring does not interfere with the viscosity extraction using the MSD at short Δt. Rather, it is a signature of the interfacial flows associated with the ongoing coarsening process during phase separation. As a result, if the goal is to

compare to bulk rheology studies, then only "equilibrated" viscosity values (lacking these flow contributions to the MSD) should be used.

Eventually, for sufficiently long aging times, convective motion subsides (Fig. 3c). For the compositions studied here involving comparatively large added salt concentrations, this typically occurs only after the samples are left undisturbed for 4–7 days. In the analysis to follow, all equilibrium microrheology data were obtained by measuring samples 4–7 days after they were mixed to ensure sufficient completion of the phase separation.

3.3 Quantifying the composition-dependence of coacervates by microrheology

To understand how the equilibrium rheology of the phase separated coacervate maps onto the equilibrium phase behavior for the PAA–PAH system, we quantify the equilibrium rheology of the PEC-dense phase using microrheology for a set of different initial compositions. The formulated compositions consist of a total of 7 polymer concentrations (C_p = 100, 200, 400, 600, 800, 1000, 1200 mM) and 4 added salt concentrations (C_s = 3, 3.5, 4, 4.5 M) (28 samples). Within this range, the PEC viscosity can be obtained by microrheology. At lower salt concentrations, the probe displacement is less than the detection limit within the experimentally accessible time frame, and the rheology is better characterized with bulk rheometry instead.[17] Macroscopic observations (*i.e.*, tilt tests) in this composition range show that the dense phase viscosity decreases with both increasing initial polymer concentration

and initial salt concentration. We further validated our microrheology analysis protocols by comparing the MSDs of centrifuged and noncentrifuged samples (Note 2.2, ESI†), of different samples at the same composition (Note 2.3, ESI†), of particles located at different z-planes (Note 2.4, ESI†). All presented no significant difference amongst them, indicating the dense phase had indeed adequately equilibrated during this time. We further compared to bulk rheology measurements and found good agreement between the two (Note 3, ESI†).

When controlling for the same total initial added polyelectrolyte concentration (C_p) and increasing the total amount of added salt (C_s), the observed microrheology data are consistent with the observation that increasing salt concentration renders the sample less viscous (Fig. 4). Specifically, as the added salt concentration increases, the magnitude of the MSD increases, indicating a decrease in dense phase viscosity. Similarly, when the polyelectrolyte concentration (C_p) is increased at fixed added salt concentration (C_s), the MSD also generally increases in magnitude, again indicating a decrease in dense phase viscosity (Fig. 5 depicts the MSD obtained at constant C_s). As we will eventually show in more detail, this decrease in viscosity with added salt is consistent with the negatively sloped tie lines observed in the equilibrium phase diagram in Fig. 2. Specifically, because the dense side of the phase boundary is negatively sloped away from the critical point, an increase in either the added polymer or salt concentration will lead to a corresponding decrease in the polymer concentration within the dense phase, resulting in a lower viscosity relative to the viscosity that would occur for a dense phase with polymer concentration equal to the initial concentration. This effect is especially pronounced at higher salt concentration where the tie lines become more negatively sloped and the polymer concentration on the dense side of the phase boundary becomes highly salt concentration-dependent (Fig. 5).
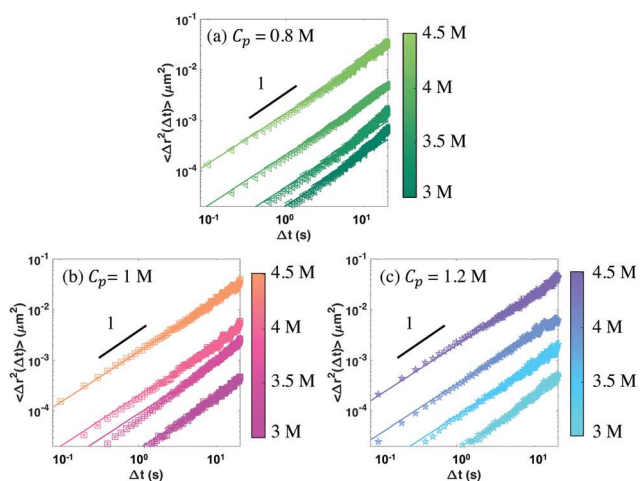

Fig. 5 Mean-squared displacement for equilibrated samples at constant added salt C_s and varying added complex C_p. Note that the exact shapes of MSDs becomes less reliable as the displacements approach the noise baseline but they are still useful in extracting the viscosity, which are shown to be comparable to that measured by bulk rheology.

An important distinction between previous reports[17] and this work for the PAA–PAH-salt system is the range of added salt concentration studied. Bulk rheology experiments reported the dense phase to be viscoelastic for this system for compositions with up to 2 M of added salt,[17] consistent with reports for many other PEC systems.[18,22,23,25] Nevertheless, application of time-salt concentration superposition produces low-frequency limiting viscous behavior, consistent with the "sticky Rouse" model, which has been proposed to describe the linear viscoelasticity of the PEC-dense phase.[18,25] The viscosity at low frequencies is the zero-shear rate viscosity η_0^*. Here, we only measure η_0^* of the dense phase by microrheology at higher salt concentrations, suggesting that any viscoelasticity of the dense phases must appear at higher frequencies (shorter lag times) than what is accessed in our measurements. Ongoing studies are aimed at resolving the viscoelastic behavior in this range. Nevertheless, the robustness of the data and the observed qualitative trends allow for a deeper quantitative examination of the composition-dependent viscosity, which will be explored in the following sections.

3.4 Relating dense-phase composition (ϕ^*, ψ^*) to the zero-shear viscosity η_0^*

Having established that the measured viscosity of the dense phase tracks the trend of relaxation time reported in earlier works,[16,17] and having directly measured the composition with established protocols,[14] we now attempt to understand the quantitative relationship between them. This dependence is elucidated by testing three different models for scaling the viscosity, for a statistically meaningful sample size accessible to our high-throughput measurements. We then empirically correlate η_0^* to polymer and salt concentrations on the dense phase boundary, using previous results of time-concentration superposition as a guide to propose scaling relationships and to

Fig. 4 Mean-squared displacement for equilibrated samples at constant C_p and varying added salt C_s. Colored data points and corresponding fit curves correspond to the concentration of added salt indicated in the color scales. The noise baseline has been measured separately (Fig. S2, ESI†) and subtracted from all measurements. Note the error bar of the variance and the fitting error are both smaller than the markers themselves.
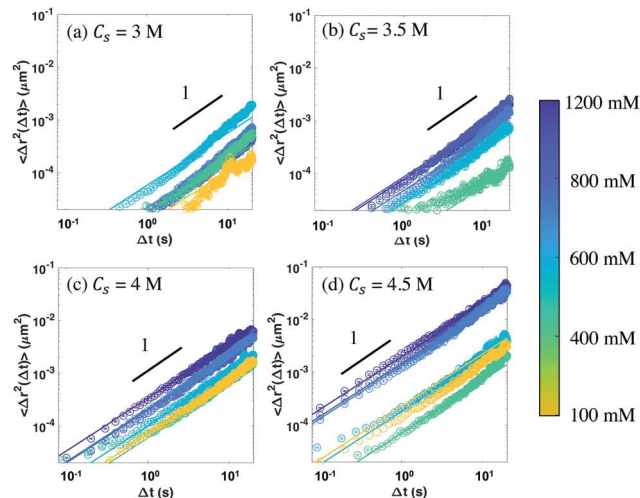
rationalize the observed changes in viscosity with composition. Thereafter, we show that it is possible to obtain a model of the equilibrium dense phase boundary with these empirical relationships and estimated parameters. We then apply several statistical tests to validate our approach and to provide guidance for future experiments.

Conventionally, many studies have found that the rheology of the dense phase in the PAA–PAH system as well as other PEC systems follows time-salt concentration superposition.[17,18,22,24] In this context, salt- and polymer-concentration dependent shift factors are used to rescale the linear viscoelastic spectrum, which exhibits a corresponding plateau modulus G_0, along both frequency (horizontal) and modulus (vertical) shift factors relative to an arbitrary reference composition. Many studies found that the vertical (modulus) shift factor is approximately a constant, while the horizontal (frequency) shift factor has a strong salt-polymer dependence, highlighting the importance of the salt concentration in setting the viscoelastic relaxation time of the fluid, τ_0. The measured terminal complex viscosity $\eta_0^* = G_0 \tau_0$ is therefore sensitive only to the horizontal shift factor. In this work, although viscoelasticity could not be observed over the captured frequency range in microrheology measurements, there is a direct link to the time-concentration superposition principle and our microrheology measurements through the measurement of η_0^*.

Comprehensive plots of the measured zero-frequency complex viscosity (Fig. 6) reveal several important observations for the analysis to follow. First, we note that the high-throughput microrheology measurements produce a large sample data set of viscosities that facilitate the testing of statistically-meaningful scaling relationships, when correlating them to the compositions measured by TGA. Second, we observe that the apparent dependence of the viscosity on polymer concentration (Fig. 6a) is relatively independent of the salt concentration; i.e., in the range studied, the viscosity data appear to collapse to a single line regardless of the added salt concentration. Finally, we note the large variation and apparent sharp dependence of viscosity on polymer concentration at the highest values of ϕ^*, which corresponds to the region of the equilibrium phase boundary where the dense-phase polymer concentration is relatively independent of the salt concentration (Fig. 2c). This suggests a difference in scaling between the high-salt concentration regime studied in this work and the low-salt concentration regime studied in previous work.[17]

Based on the various analyses of PAA:PAH rheology performed previously, we simultaneously consider three models. Model 1 uses a power law[48,49] of polymer concentration to explain the observed viscosity variation (Fig. 6a):

$$\eta_0^*(\phi^*) = C_1(\phi^*)^\beta. \tag{1}$$

On the other hand, Fig. 6b suggests the following relationship between viscosity and the salt concentration, as given by Model 2:

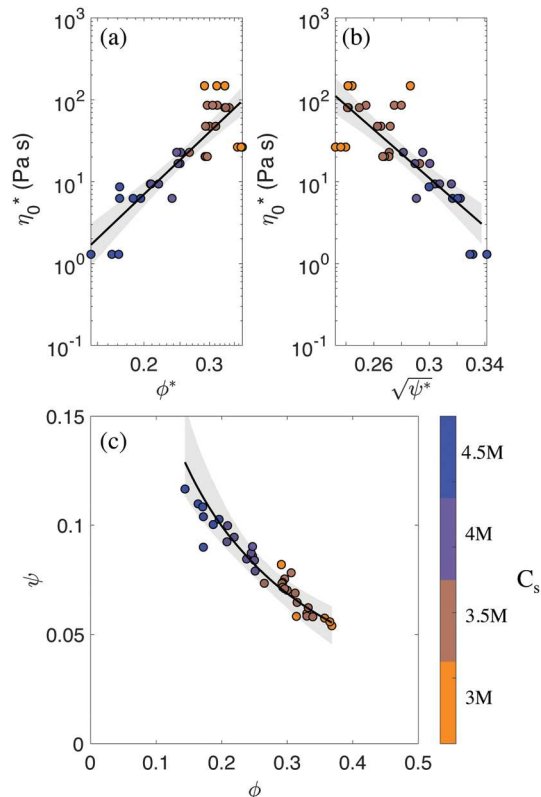$$\eta_0^*(\psi^*) = C_2 \exp\left(-A\sqrt{\psi^*}\right). \tag{2}$$

Fig. 6 (a and b) Linear model fitting for relationship between viscosity and composition. (c) Reconstructed phase boundary using fitted model. The 95% confidence interval of the fitting for each case is denoted by the grey shaded area. The color bar denotes different added salt concentration C_p corresponding to each point.

We also consider the joint dependence of the viscosity on the polymer and salt concentration in Model 3:[24,25]

$$\eta_0^*(\phi^*, \psi^*) = C_3(\phi^*)^{\bar{\beta}} \exp\left(-\tilde{A}\sqrt{\psi^*}\right). \tag{3}$$

After taking the logarithm of the viscosity, Model 1–3 expressed in eqn (1)–(3) can be fit by linear regression (detailed fitting procedure can be found in Note 6.2 in ESI†). We find that the fit by only using polymer concentrations (eqn (1)) has a very similar adjusted coefficient of determination (R_{adj}^2) to that obtained using both polymer and salt concentrations (eqn (3) and Table 1). The large p-value in testing whether the linear coefficient of salt concentration $\tilde{A} = 0$ in eqn (3) indicates that we cannot reject the null hypothesis that $\tilde{A} = 0$, which is identically equal to the case where the viscosity is independent of the salt concentration (Model 1) along the dense phase boundary. The analysis therefore indicates that the zero-shear viscosity of compositions along the phase boundary is dominated by the polymer concentration. Furthermore, for fixed polymer concentration, we find that the salt concentration is significant for fitting the viscosity using Model 2 (Table 1). This is because the salt concentration is negatively correlated with polymer concentration for compositions along the dense phase boundary (i.e., the phase boundary is negatively sloped). In

Table 1 Linear regression model for viscosity. The adjusted coefficient of determination is denoted by R_{adj}^2. Models 1–3 correspond to linear regression models from eqn (1)–(3). The name of the parameters, fitted values and 95% confidence intervals are shown in column 2–4. The t-statistics for testing whether the linear regression coefficient is zero, its p-value and significance levels are given in column 5–7. A small p-value indicates the corresponding linear coefficient is significantly different from zero

	Param.	Fitted	95% C.I.	t-value	p-value	Sig. level
Model 1	$\log(C_1)$	9.1	[7.8, 10.4]	14.3	1.9×10^{-15}	***
$R_{adj}^2 = 0.74$	β	4.5	[3.5, 5.5]	9.6	5.6×10^{-11}	***
Model 2	$\log(C_2)$	12.6	[10.1, 15.2]	10.1	1.71×10^{-11}	***
$R_{adj}^2 = 0.64$	A	34.0	[25.0, 43.0]	7.7	9.0×10^{-9}	***
Model 3	$\log(C_3)$	7.2	[3.5, 10.9]	3.9	4.6×10^{-4}	***
$R_{adj}^2 = 0.74$	β	6.4	[2.8, 10.0]	3.6	1.0×10^{-3}	**
	$\tilde{A}$	-15.9	$[-45.1, 13.0]$	-1.1	0.27	

Sig. codes: '***' = 0–0.001, '**' = 0.001–0.01, '*' = 0.01–0.05, no symbol = 0.1–1.0

summary, for the range of compositions studied, for a given polymer concentration, the observed viscosity is statistically insensitive to the salt concentration, such that any cross-dependence can be safely ignored for these conditions.

Having established the separability of polymer- and salt-dependence of the viscosity along the dense phase boundary in the model system studied, we compare the observed scalings to those previously reported in the literature. Power law scaling of viscosity with volume fraction is observed across a range of polymer fluids including polyelectrolytes and PECs.[22,23] We note that β is not necessarily invariant to polymer concentration; instead, it may increase as ϕ increases due to the increasing inter-chain association.[49] Nevertheless, for the ranges examined here, an average value of $\beta = 4.5$ ([3.5, 5.5]) adequately describes the trend observed in the data (Fig. 6a). Similar values of β extracted from viscoelastic shift factors using time-concentration superposition were reported in[24] for compositions above the equilibrium phase boundary. The observed scaling with salt concentration described by eqn (2) is consistent with the scaling proposed previously for an effective salt friction coefficient, $\zeta(\psi) \sim \exp\left(-a(T)\sqrt{C_s(\psi)}\right)$,[12,18,25,50] where C_s denotes the molarity of salt, and the constant $a(T)$ can be inferred from system parameters:[17,18]

$$a(T) = \frac{\sqrt{2000 N_A}e^3}{2\pi(\varepsilon\varepsilon_0 k_B T)^{1.5}}, \quad (4)$$

where N_A is Avogadro's number, e is the fundamental charge, ε_0 and ε are the vacuum permittivity and relative permittivity of the medium, k_B is the Boltzmann constant, and T denotes the absolute temperature. Thus, $a(T) = 1.68 \times 10^7 T^{-1.5}\varepsilon^{-1.5}\left[=\frac{1}{\sqrt{M}}\right]$ is a constant. $\zeta(\psi)$ assumes that the longest viscoelastic relaxation time τ_0 is dominated by exchange of polymer-bound ions between polymer-polymer and polymer-free ion aggregates, with an activation energy based on the Debye–Hückel theory for screened electrostatics. In eqn (4), ε varies from 80 at 0 M salt, to about 45–50 at 3–4.5 M at $T = 298$ K.[51,52] Thus, $a(T)$ is a constant ranging from $4.56 - 9.24\frac{1}{\sqrt{M}}$ for the salt concentrations

considered. We derive a value of the coefficient A in model (2) of $A = 34.0$ ([25.0, 43.0]) from a linearized fit of the data, and given a conversion factor of 1 M = 0.0269 v/v for water, we arrive at $a(t) = 5.61 \pm 0.71\frac{1}{\sqrt{M}}$, well within the estimated range. This value of A is also comparable to $4.74\frac{1}{\sqrt{M}}$, the reported shift factor from bulk rheology data reported by[17] for the same system.

We perform out-of-sample testing (Note 6.4, Fig. S10, ESI†), where 2/3 of the data were used to construct the linear model and the other 1/3 were withheld for testing. This test indicates that the empirical relationships $\eta_0^*(\phi^*), \eta_0^*(\psi^*)$ do an excellent job at predicting η_0^* for ϕ^* and ψ^* in the validation set, indicating the robustness of the model. We also performed a sensitivity analysis on various fitting parameters (Note, 6.5, Table S2, ESI†) using 25%, 50% and 75% of the data to find the fitting parameters, and find that in practice, as little as 50% of the data used in our study are needed to ensure precision of the parameter values. This means that approximately 15 unique viscosity and composition measurements, based on the accuracy required, would be necessary to obtain a statistically equivalent, empirical mapping from viscosity to the composition on the phase boundary, significantly reducing the time cost associated with measuring the composition by TGA.

3.5 Reconstructing the dense phase boundary by viscosity

We will now show the utility in gathering a large microrheology data set by demonstrating how it can be used to estimate the location of the PEC-dense phase boundary within the PAA–PAH phase diagram without the need for TGA measurements and their associated time and material cost. Specifically, by equating the viscosity in the empirical scalings of eqn (1) and (2) and their determined best-fit model parameters, it can be shown that, if A, β, C_1 and C_2 are all assumed to be constants over the range of analysis (as we have done so far), and they all are positive-valued (which they must to be physically meaningful), then η_0^* can be eliminated in the equations to leave an algebraic relationship for ψ^* in terms of ϕ^*,

$$\psi^* = \frac{1}{A^2}\left[\log\left(\frac{C_2}{(\phi^*)^\beta C_1}\right)\right]^2 \quad (5)$$

In other words, inversion of the scaling relationships for viscosity with ϕ^* and ψ^* along the PEC-dense phase boundary produces an empirical function for the boundary itself. We show additional analysis by taking the first and second derivatives, $\frac{\partial \psi^*}{\partial \phi^*}$ and $\frac{\partial^2 \psi^*}{\partial(\phi^*)^2}$ (Note 6.6, ESI†) to understand resulting curvature of the boundary. For the particular best-fit values of A and β and their confidence intervals, we find that the resulting phase boundary is indistinguishable from a locally flat (i.e., linear) shape.

Having established a procedure to estimate the equilibrium phase boundary from a large set of viscosity measurements, we now assess the accuracy of the analysis by comparing these estimates to the more direct measurements of the phase boundary and its associated tie lines obtained from TGA experiments (Fig. 7). To map the viscosity to composition, we first derive the expressions relating η_0^* to ϕ^* and ψ^* by
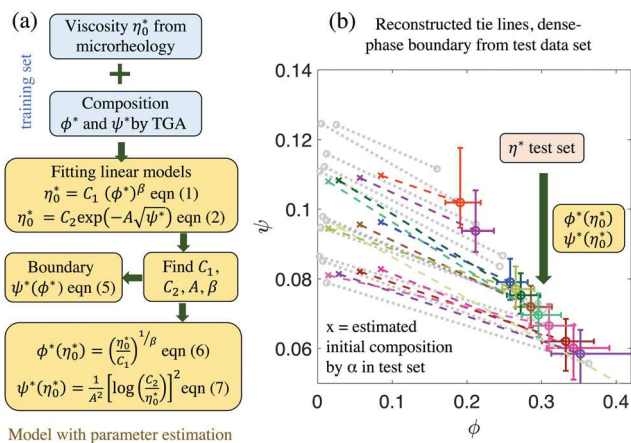
Fig. 7 (a) Process flow to extract the model parameters using composition and viscosity of data in the model fitting set. (b) Reconstructed dense phase compositions with uncertainty and tie lines by connecting each set of the initial composition and the PEC-dense phase composition. Measured PEC composition and tie lines (model fitting set) are shown in grey circles and dotted lines. The initial compositions (validation set) are shown in colored "x". Using η_0^* and the model, PEC-rich phase compositions of the validation set are constructed by open circles.

rearranging eqn (1) and (2):

$$\phi^*\left(\eta_0^*\right) = \left(\frac{\eta_0^*}{C_1}\right)^{\frac{1}{\beta}}, \tag{6}$$

$$\psi^*\left(\eta_0^*\right) = \frac{1}{A^2}\left[\log\left(\frac{C_2}{\eta_0^*}\right)\right]^2. \tag{7}$$

These expressions together with the the fitting constants A, β, C_1, C_2 derived from fitting the linear models (Fig. 6a and b) to the model fitting set, constitute the model with estimated parameters (Fig. 7a), which will be applied to a new set of data (the validation set), for which η_0^* has been measured by microrheology, but $(\phi\star, \psi\star)$ have not been measured by TGA. The composition will thus be derived from the model instead.

First, the initial compositions are estimated by the apparent degree of ionization $\alpha = 0.13$ (Fig. 2), denoted as "x" in Fig. 7b. Then, estimated compositions along the dense-phase boundary by η_0^* are denoted by the filled circles in Fig. 7c. Finally, a dashed line of the same color connecting the initial and final compositions constitute an estimate for the tie lines at the PEC-dense phase state points estimated from the measured viscosity. All η_0^* used in this case fall within the range for which the fitting was performed in the last Section, but none were used in the fitting procedure. TGA measurements from the model fitting set (first shown in Fig. 2) also appear as grey dotted lines in the plot to facilitate comparison with the directly measured phase behavior (Fig. 7).

Overall, we find that, in the absence of the TGA measurements, the dense phase composition and the tie lines can both be reconstructed to a remarkable degree solely by measurements of the viscosity, using the trained relationships between viscosity and composition (which, we note, are ignorant of the underlying phase separation). While the validation set is not in any way related to the data used in the model fitting set, thermodynamics dictate that initial compositions falling on the same tie line would result in the same PEC composition. Therefore, the tie lines for the two sets of data bear striking resemblance to each other. Our method therefore greatly reduces the time cost associated with characterizing the phase diagram for any new samples in this material system.

4 Conclusions

We have demonstrated an *in situ*, high-throughput microscopy platform and associated analysis workflow to simultaneously track the evolution and aging of structure and microrheology in complex fluids undergoing phase separation. The advantages of the method, which include small sample volumes, automated data acquisition, the ability to track time-evolving processes and simultaneously obtain morphological and rheology information, and time and cost reduction associated when constructing the phase diagram by TGA through the use of statistical models.

These advantages were emphasized by applying the method to mixed polyelectrolyte solutions undergoing coacervation-driven liquid–liquid phase separation. In particular, we showed that the method allows measurements of material properties close to the critical point, which is otherwise difficult to access using conventional methods by obviating the need to separate the emerging phases for *ex situ* characterization. The large data sets obtained facilitate analysis to estimate the relationship between composition and viscosity using a phenomenological scaling model. We demonstrate that this data-driven model can be inverted to estimate equilibrium phase behavior, which is in quantitative agreement with direct measurements using conventional TGA approaches. The new experimental capabilities enabled by the high-throughput approach provide an effective tool to formulate multi-phase complex fluids, and to explore the the underlying processes of phase separation from micro- to macroscopic scales.

Author contributions

MEH, MTV, YL and CERE designed the project. YL and CERE performed experiments. YL and MG performed numerical modeling and analysis. YL, MEH, MTV, MG, and CERE wrote the manuscript. All authors have given approval to the final version of the manuscript.

Conflicts of interest

There are no conflicts to declare.

Acknowledgements

References

1 A.-V. G. Ruzette and A. M. Mayes, *Macromolecules*, 2001, **34**, 1894–1907.

2 D. Aarts and H. Lekkerkerker, *J. Phys.: Condens. Matter*, 2004, **16**, S4231.

3 Y. Gao, J. Kim and M. E. Helgeson, *Soft Matter*, 2015, **11**, 6360–6370.

4 E. R. Dufresne, H. Noh, V. Saranathan, S. G. Mochrie, H. Cao and R. O. Prum, *Soft Matter*, 2009, **5**, 1792–1795.

5 L. Li, X. Shen, S. W. Hong, R. C. Hayward and T. P. Russell, *Angew. Chem.*, 2012, **124**, 4165–4170.

6 S. Mani, M. F. Malone and H. H. Winter, *J. Rheol.*, 1992, **36**, 1625–1649.

7 H. Tanaka, *Phys. Rev. Lett.*, 1996, **76**, 787.

8 S. Alberti, A. Gladfelter and T. Mittag, *Cell*, 2019, **176**, 419–434.

9 I. Kaminker, W. Wei, A. M. Schrader, Y. Talmon, M. T. Valentine, J. N. Israelachvili, J. H. Waite and S. Han, *Soft Matter*, 2017, **13**, 9122–9131.

10 S. Turgeon, C. Schmitt and C. Sanchez, *Curr. Opin. Colloid Interface Sci.*, 2007, **12**, 166–178.

11 C. E. Sing and S. L. Perry, *Soft Matter*, 2020, **16**, 2885–2914.

12 A. B. Marciel, S. Srivastava and M. V. Tirrell, *Soft Matter*, 2018, **14**, 2454–2464.

13 L. Li, S. Srivastava, M. Andreev, A. B. Marciel, J. J. de Pablo and M. V. Tirrell, *Macromolecules*, 2018, **51**, 2988–2995.

14 L. Li, S. Srivastava, S. Meng, J. M. Ting and M. V. Tirrell, *Macromolecules*, 2020, **53**, 7835–7844.

15 W. C. B. McTigue, E. Voke, L.-W. Chang and S. L. Perry, *Phys. Chem. Chem. Phys.*, 2020, **22**, 20643–20657.

16 C. E. R. Edwards, K. L. Lakkis and M. E. Helgeson, *Submitted*, 2022, Submitted.

17 V. M. Syed and S. Srivastava, *ACS Macro Lett.*, 2020, **9**, 1067–1073.

18 E. Spruijt, M. A. Cohen Stuart and J. van der Gucht, *Macromolecules*, 2013, **46**, 1633–1641.

19 M. Tekaat, D. Bütergerds, M. Schönhoff, A. Fery and C. Cramer, *Phys. Chem. Chem. Phys.*, 2015, **17**, 22552–22556.

20 Y. Liu, C. F. Santa Chalarca, R. N. Carmean, R. A. Olson, J. Madinya, B. S. Sumerlin, C. E. Sing, T. Emrick and S. L. Perry, *Macromolecules*, 2020, **53**, 7851–7864.

21 E. Spruijt, A. H. Westphal, J. W. Borst, M. A. Cohen Stuart and J. van der Gucht, *Macromolecules*, 2010, **43**, 6476–6484.

22 R. G. Larson, Y. Liu and H. Li, *J. Rheol.*, 2021, **65**, 77–102.

23 Y. Liu, H. H. Winter and S. L. Perry, *Adv. Colloid Interface Sci.*, 2017, **239**, 46–60.

24 F. J. Morin, M. L. Puppo and J. E. Laaser, *Soft Matter*, 2021, **17**, 1223–1231.

25 E. Spruijt, J. Sprakel, M. Lemmers, M. A. C. Stuart and J. Van Der Gucht, *Phys. Rev. Lett.*, 2010, **105**, 208301.

26 J. McCarty, K. T. Delaney, S. P. Danielsen, G. H. Fredrickson and J.-E. Shea, *J. Phys. Chem. Lett.*, 2019, **10**, 1644–1652.

27 R. S. Fisher and S. Elbaum-Garfinkle, *Nat. Commun.*, 2020, **11**, 1–10.

28 K. A. Black, D. Priftis, S. L. Perry, J. Yip, W. Y. Byun and M. Tirrell, *ACS Macro Lett.*, 2014, **3**, 1088–1091.

29 J. J. Madinya, L.-W. Chang, S. L. Perry and C. E. Sing, *Mol. Syst. Des. Eng.*, 2020, **5**, 632–644.

30 L.-W. Chang, T. K. Lytle, M. Radhakrishna, J. J. Madinya, J. Vélez, C. E. Sing and S. L. Perry, *Nat. Commun.*, 2017, **8**, 1–8.

31 E. M. Furst and T. M. Squires, *Microrheology*, Oxford University Press, 2017.

32 T. M. Squires and T. G. Mason, *Annu. Rev. Fluid Mech.*, 2010, **42**, 413–438.

33 S. Elbaum-Garfinkle, Y. Kim, K. Szczepaniak, C. C.-H. Chen, C. R. Eckmann, S. Myong and C. P. Brangwynne, *Proc. Natl. Acad. Sci. U. S. A.*, 2015, **112**, 7189–7194.

34 L. Jawerth, E. Fischer-Friedrich, S. Saha, J. Wang, T. Franzmann, X. Zhang, J. Sachweh, M. Ruer, M. Ijavi and S. Saha, *et al.*, *Science*, 2020, **370**, 1317–1323.

35 S. Park, R. Barnes, Y. Lin, B.-J. Jeon, S. Najafi, K. T. Delaney, G. H. Fredrickson, J.-E. Shea, D. S. Hwang and S. Han, *Commun. Chem.*, 2020, **3**, 1–12.

36 R. Chollakup, W. Smitthipong, C. D. Eisenbach and M. Tirrell, *Macromolecules*, 2010, **43**, 2518–2528.

37 Y. Gao and M. L. Kilfoil, *Opt. Express*, 2009, **17**, 4685–4704.

38 J. C. Crocker and D. G. Grier, *J. Colloid Interface Sci.*, 1996, **179**, 298–310.

39 M. Gu, Y. Luo, Y. He, M. E. Helgeson and M. T. Valentine, *Phys. Rev. E*, 2021, **104**, 034610.

40 N. Bobroff, *Rev. Sci. Instrum.*, 1986, **57**, 1152–1157.

41 T. Savin and P. S. Doyle, *Biophys. J.*, 2005, **88**, 623–638.

42 R. Chollakup, J. B. Beck, K. Dirnberger, M. Tirrell and C. D. Eisenbach, *Macromolecules*, 2013, **46**, 2376–2390.

43 J. T. G. Overbeek and M. Voorn, *J. Cell. Comp. Physiol.*, 1957, **49**, 7–26.

44 A. E. Neitzel, Y. N. Fang, B. Yu, A. M. Rumyantsev, J. J. de Pablo and M. V. Tirrell, *Macromolecules*, 2021, **54**, 6878–6890.

45 D. Priftis and M. Tirrell, *Soft Matter*, 2012, **8**, 9396–9405.

46 D. Priftis, X. Xia, K. O. Margossian, S. L. Perry, L. Leon, J. Qin, J. J. de Pablo and M. Tirrell, *Macromolecules*, 2014, **47**, 3076–3085.

47 H. Tanaka, *J. Phys.: Condens. Matter*, 2000, **12**, R207.

48 H. H. Winter and F. Chambon, *J. Rheol.*, 1986, **30**, 367–382.

49 M. Rubinstein and A. N. Semenov, *Macromolecules*, 2001, **34**, 1058–1068.

50 F. G. Hamad, Q. Chen and R. H. Colby, *Macromolecules*, 2018, **51**, 5547–5555.

51 J. Hasted, D. Ritson and C. Collie, *J. Chem. Phys.*, 1948, **16**, 1–21.

52 N. Gavish and K. Promislow, *Phys. Rev. E*, 2016, **94**, 012611.